Medial Techniques to Automate Finite Element Analysis of Prostate Deformation

Jessica Crouch, Stephen M. Pizer, *Senior Member, IEEE,* Edward L. Chaney, Marco Zaider

***Abstract*— Finite element analysis provides a principled method for modeling physical deformation and is an ideal tool to apply when a medical imaging problem requires the simulation of tissue deformation. The drawback to using finite element analysis for imaging problems is the labor and computational time that is required to construct a finite element model and solve the resulting large system of equations. Challenging questions include how to (1) generate a mesh from an image, (2) derive boundary conditions from images of deformed objects, and (3) solve the system of finite element equations efficiently. This work addresses these questions with algorithms based on medial models called m-reps. A multiscale meshing algorithm is presented that automatically generates a hexahedral mesh from an m-rep segmentation of an image, and an m-rep based method for establishing boundary conditions is described. Additionally, an efficient solution algorithm is presented that takes advantage of the multi-scale nature of the problem. Together, these m-rep based algorithms improve the automation and efficiency of FEM for non-rigid registration problems. Initial results are presented for the registration of CT images of a prostate phantom.**

***Index Terms*— registration, elastic, finite element, m-rep, prostate**

I. Introduction

FINITE element analysis has proven useful in solving medical imaging problems for which deformation is significant. Most notably, this approach has yielded positive results for same-subject non-rigid image registration and for medical simulation applications. Published results include image registration for the prostate [1] [2], brain [3] [4] [5] [6], and breast [7] [8], as well as simulation of maxillo-facial surgery [9], liver surgery [10], and childbirth [11].

The work presented here is potentially applicable to the variety of medical imaging applications that require deformation modeling. The particular application considered here is non-rigid registration of prostate images that are used for brachytherapy planning and guidance. Brachytherapy involves implanting radioactive seeds in the prostate to treat prostate cancer. Research is underway to determine whether brachytherapy outcomes can be improved by placing the radioactive seeds in a pattern that concentrates the radiation dose to areas of the prostate that have elevated levels of choline and citrate, two chemicals believed to indicate tumor presence. These prostate levels can be determined from a magnetic resonance spectroscopy image (MRSI) that is acquired using an intra-rectal imaging probe. An MRSI can be used to design a seed placement pattern that targets the suspected tumor deposits, but the process is complicated by the fact that the prostate appears compressed in the MRSI due to pressure from the imaging probe. Intra-operatively, the prostate is not deformed by the MRSI probe and seed placement is guided using ultrasound. Therefore, image registration is required to match the planning image with the intra-operative image.

Other researchers have approached prostate registration using both rigid [12] [13] and non-rigid [14] methods. Studies have shown that for brachytherapy planning and treatment the magnitude of prostate deformation is large enough that it should not be ignored [15]. Since the deformation that occurs over the course of brachytherapy treatment is predominantly due to mechanical forces, finite element based registration approaches are especially appropriate. Previous finite element based prostate registration work includes [1] and [2]. The work presented in [1] is most similar to the algorithm presented here, but differs from this work in that it relied on manual segmentation and tetrahedral meshing, and a membrane model of the boundary rather than a solid object model was used in the computation of boundary conditions. The work presented in [2] employed a combined statistical and biomechanical approach, while the work presented here relies on medial geometry and biomechanics to generate a deformation. The consistent use of a medial model framework to automate the application of finite element analysis is a feature, described in the next section, that sets this work apart from previous work.

As computational power has grown more available, finite element analysis has become a more accessible tool for medical imaging research. However, its application is often limited to the research arena due to significant costs of user time for finite element model construction and computational time for deformation calculations. This work focuses on specific techniques to make finite element analysis more automatic and efficient for medical imaging applications. Reducing the amount of human and computer time required to employ finite element analysis will make it a more attractive and practical tool for both research and clinical applications.

M-rep object models can efficiently represent organ shape, and they carry with them an automated way of defining a finite element mesh and boundary conditions. Therefore m-reps are a useful tool for automating the modeling of organ deformation. For prostate image registration, the m-rep based deformation modeling process consists of the following steps.

1) Fit a single medial model (m-rep), to both the prostate in the undeformed image and the prostate in the deformed image. The m-rep fitted to the undeformed prostate is

Manuscript received February 1, 2003; revised October 28, 2003. Financial support for this work was provided by NIH grants CA P01 47982 and EB P01 02779 and by a Lucent Foundation GRPW fellowship.

J. Crouch, S. Pizer, and E. Chaney are with the Medical Image Display and Analysis group at the University of North Carolina, Chapel Hill

M. Zaider is with Memorial Sloan-Kettering Cancer Center

referred to as the $model$, and the m-rep fitted to the deformed prostate is referred to as $model'$.
2) Build a finite element mesh from the $model$.
3) Derive finite element boundary conditions that deform $model$ into $model'$ and minimize the energy of the deformation.
4) Use a linear elastic mechanical model and compute the deformation to the desired precision by solving the finite element system of equations on a coarse mesh and iteratively subdividing the mesh and solving the equations on the finer mesh.
5) Apply the computed deformation to the undeformed image to register it with the deformed image.

Section II details how m-rep object models are used to automatically generate a mesh from an image. The method for determining boundary conditions from a pair of m-rep models is explained in section III. An efficient solution algorithm is presented in section IV. Results of this process applied to CT images of a prostate phantom are given in section V, and future work is discussed in section VI.

II. Meshing Algorithm

The novel meshing algorithm presented here relies on m-rep object models to provide both global and local object shape information. An overview of m-rep models is presented, followed by an explanation of the meshing algorithm.

A. M-Rep Models

The medially based object representation introduced by Blum [16] consists of a medial surface and a radius function defined on the medial surface. The intuitive picture is of spheres of maximal diameter fit inside an object so that they touch both sides of the object's boundary. The center point of each such sphere is a point on the medial surface, and the radius of each sphere defines the radius function at that point on the medial surface. The medial surface branches to represent object protuberances. See Fig. 1 for an illustration.

In the general case, an m-rep consists of a hierarchical tree of figures, where each figure represents a branch of the medial surface. The simplest m-rep consists of a single figure that represents a slab-like region with a non-branching medial locus. Because the prostate's shape can be well represented with a single figure m-rep, the discussion of m-reps here will be limited to single figure models. Readers are referred to [17] for a more thorough explanation of m-reps, including multi-figure models.

A figure is represented by a lattice of medial atoms, each of which provides a sample of object geometry at a point. Fig. 2

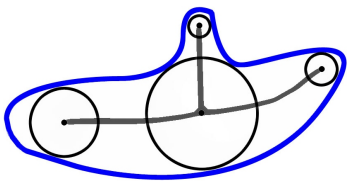

Fig. 1. This 2D figure is inscribed with circles of maximal diameter and illustrated a branched medial axis.

illustrates the structure of a medial atom and a figure. Medial atoms are the smallest building blocks of an m-rep, and each stores the following information:

- $\mathbf{x}$, the position of the medial sheet at a sample point
- r, the radius, which is defined as the distance from $\mathbf{x}$ to the object boundary
- two vectors that originate at $\mathbf{x}$ and point to the boundary locations that an inscribed sphere at $\mathbf{x}$ with radius r would touch
- $F = (\vec{n}, \vec{b}, \vec{b}^{\perp})$, a frame that defines the tangent plane of the medial sheet at $\mathbf{x}$. The direction $\vec{b}$ on the tangent plane is in the $-\nabla r$ direction, $\vec{n}$ is the normal to the medial sheet, and $\vec{b}^{\perp}$ is the cross product of $\vec{b}$ and $\vec{n}$.
- θ, the angle between $\vec{b}$ and a boundary vector

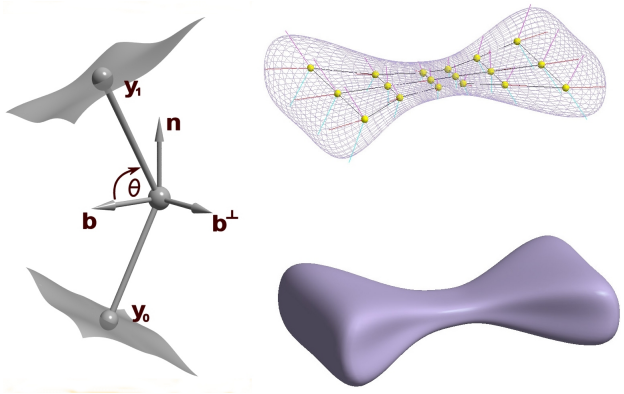

Fig. 2. Left: A diagram of a single medial atom with object properties labelled. Right Top: A single figure m-rep model composed of a lattice of medial atoms Right Bottom: M-rep with solid object surface rendering

The lattice arrangement of medial atoms helps to define the object based coordinate system for m-reps. Any point in an object can be referenced by its m-rep defined (u, v, t, τ) coordinates. The u and v directions coincide with the rows and columns of medial atoms in the lattice. τ ranges between 0 at the medial surface and ± 1 at the object surface, while t measures a fraction of the angle between $+\theta$ and $-\theta$ in the crest region of the object. Interpolation is applied to generate continuous functions that represent the coordinates of a figure's medial sheet, boundary, radius, and other atom properties. Through this interpolation process, (u, v, t, τ) coordinates can be mapped to world space (x, y, z) coordinates. The following function represents this mapping operation:

$$[x_i \;\; y_i \;\; z_i] = MedialToWorld(model,\, u_i,\, v_i,\, t_i,\, \tau_i) \quad (1)$$

The object based coordinate system provides spatial and orientational correspondence between deformed versions of the same object (Fig. 3). For example, given a prostate m-rep model that has been fitted to both a compressed prostate image and an uncompressed prostate image, a set of (u, v, t, τ) coordinates applied to both model configurations will reference approximately the same part of the prostate tissue in each. The object based coordinates establish a geometry based correspondence that approximates the physical correspondence but is not identical to the physical correspondence. A geometry based registration can be performed using these correspondences, but experiments show that a physically based finite

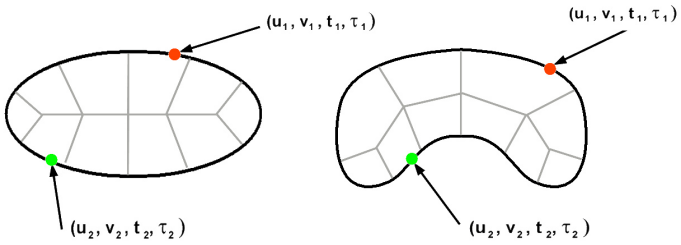

Fig. 3. The m-rep figure on the right is a deformed version of the figure on the left. The m-rep object coordinate system that is shared by both versions of the figure establishes a correspondence between boundary points. (u_1, v_1, t_1, τ_1) and (u_2, v_2, t_2, τ_2) mark two sets of corresponding points.

element model provides better registration accuracy than m-rep correspondences. These results are presented in Fig. 13.

One advantage of the object based coordinate system is that a mesh defined using an m-rep's object based coordinates is automatically individualized to fit any deformed version of the m-rep model. This occurs because the mesh's object based coordinates do not change with deformation; only the mapping between object coordinates and world space changes when the m-rep is deformed. Another benefit of the object based coordinate system is the ability to express distances as a fraction of object width. This is convenient for mesh generation as it provides a natural way to size elements according to the proportions of an object.

In addition to the advantages offered by object based coordinates, m-reps are particularly attractive as part of an automatic meshing algorithm because they can be used to automatically segment objects from images [17]. In this work m-reps form a critical link between the image and the mesh generation process. Through an automatic segmentation procedure m-rep models are fit to image data, and then the geometry information stored in the m-rep is used to automatically generate a high quality finite element mesh.

An m-rep model building program named *Pablo* has been developed by the Medical Image Display and Analysis Group group at the University of North Carolina at Chapel Hill. This software can generate m-rep models, and it allows editing of the position, radius, and other properties of individual medial atoms. Pablo also has the capability to automatically fit an m-rep to image data. It uses a conjugate gradient algorithm to adjust the medial atom properties so that the boundary match between an m-rep model and a visible boundary in an image is maximized, subject to certain geometric constraints. All of the m-rep models presented in this paper were created and fitted to images using Pablo.

B. Hexahedral Meshing Algorithm

For many finite element applications meshes constructed with hexahedral elements are preferable to meshes built from tetrahedral elements due to their superior convergence and accuracy characteristics. Research has shown that for both linear elastic and non-linear elasto-plastic problems the error in a finite element solution is smaller for a mesh of linear hexahedral elements than for a mesh of similarly sized linear tetrahedral elements [18]. However, currently available automatic meshing algorithms are more successful at constructing quality tetrahedral meshes than quality hexahedral meshes. Some research has been directed toward the development of hexahedral meshes from images [19], but the development of automatic hexahedral meshing algorithms is a challenging problem that continues to motivate current research efforts in the meshing community [20].

An automatic hexahedral meshing algorithm based on m-reps has been developed and is summarized here. Readers are referred to [21] and [22] for details on this meshing method.

The single figure version of the m-rep based meshing algorithm uses a standard meshing pattern for each figure of a model and assigns object based coordinates to each node. The mapping from object based coordinates to world space coordinates determines the nodes' placement in world space. The single figure meshing procedure is illustrated in Fig. 4.

The first step in meshing a m-rep figure is the construction of a sampling grid on the (u, v) parameter plane of the medial surface. The vertices of the sampling grid are placed at regular intervals in (u, v) coordinates, as shown in Figs. 4b and 4c.

From the sampling grid on the medial surface the coordinates of the other layers of nodes can be derived. For every (u, v) sample point except those around the outer rim of the medial atom lattice, five nodes are created at $\tau = -1, -.5, 0, .5, 1$. For sample points in that rim, a slightly different set of six nodes is created, with the sixth node sitting out on the object crest. The resulting mesh pattern is illustrated in Fig. 4d. The mesh construction is guided entirely by information contained in the m-rep model, so the meshing process requires no user interaction.

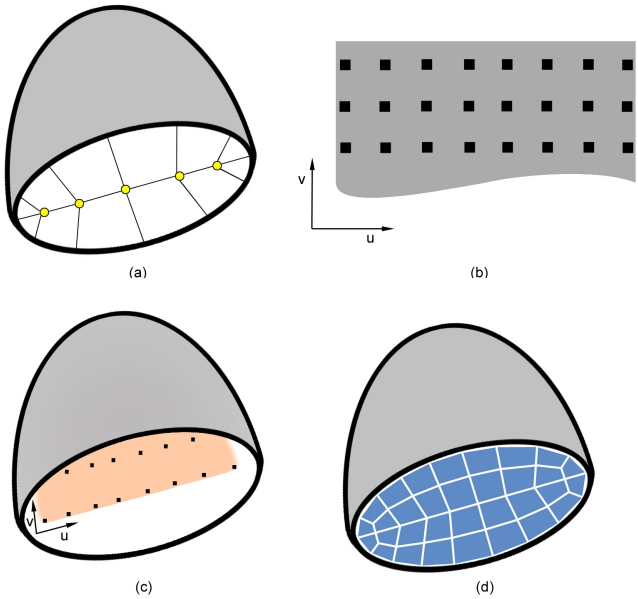

Fig. 4. (a) The m-rep defines and parameterizes the object's medial surface. (b) A regular sampling grid is defined in the (u,v) parameter space of the medial surface. (c) The regular sampling grid is mapped into world space. (d) Each sample point on the medial surface gives rise to a group of mesh nodes. For the center region, each sample point leads to 5 nodes placed at constant u and v and evenly spaced τ.

C. Mesh Quality Optimization

A three dimensional isoparametric element is defined in a parameter space (Fig. 5a) and is mapped into world space (Fig. 5b) via the element shape function $(x, y, z) = N(\xi, \eta, \zeta)$. For an 8-node isoparametric linear hexahedral element, the shape function is defined as follows [23].

$$N(\xi,\eta,\zeta) = \sum_{i=1}^{8} N_i(\xi,\eta,\zeta)\cdot[x_i y_i z_i] \quad (2)$$

where $[x_i y_i z_i]$ are the coordinates of node i and N_i is defined as

$$\begin{aligned} N_1 &= \tfrac{1}{8}(1-\xi)(1-\eta)(1-\zeta) & N_2 &= \tfrac{1}{8}(1+\xi)(1-\eta)(1-\zeta) \\ N_3 &= \tfrac{1}{8}(1+\xi)(1+\eta)(1-\zeta) & N_4 &= \tfrac{1}{8}(1-\xi)(1+\eta)(1-\zeta) \\ N_5 &= \tfrac{1}{8}(1-\xi)(1-\eta)(1+\zeta) & N_6 &= \tfrac{1}{8}(1+\xi)(1-\eta)(1+\zeta) \\ N_7 &= \tfrac{1}{8}(1+\xi)(1+\eta)(1+\zeta) & N_8 &= \tfrac{1}{8}(1-\xi)(1+\eta)(1+\zeta) \end{aligned} \quad (3)$$

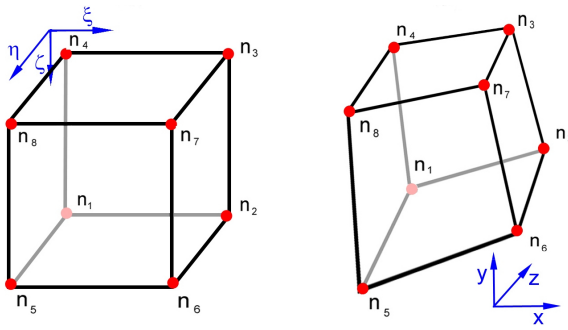

Fig. 5. Left: Hexahedral element in its (ξ, η, ζ) parameter space Right: Hexahedral element that has been mapped into world space

Whether a valid finite element solution exists on a mesh depends on J, the Jacobian of the shape function $N(\xi, \eta, \zeta)$. Although a solution can be computed as long as the measure of element volume, det(J), is non-negative [24], when det(J) is scaled to the interval [-1, 1] desirable elements have a value of at least 0.5. Smaller det(J) values are associated with strongly distorted elements that can negatively impact the condition number of the finite element stiffness matrix and reduce the accuracy of the computed solution. It is sufficient to check the det(J) values at the Gauss integration points in each element [25]. The computation of the stiffness matrix involves the numerical evaluation of an integral over the volume of the entire mesh, and the Gauss integration points are the locations inside each element where this integral is evaluated.

As gauged by det(J), the element quality of the majority of hexahedral elements generated by the m-rep based meshing algorithm is good, but some elements generated near the corners of the parameterized medial surface or in areas of higher curvature can have poorer shape. Therefore, after mesh construction an optimization is performed to improve the shape of the less desirable elements.

The mesh quality improvement procedure first assigns to each element a score that is the minimum value of det(J) evaluated at each of the Gauss integration points in the element. A list is compiled of all elements with det(J) values less than .5 and the immediate neighbors of those elements. For each element on the list, the coordinates of its nodes

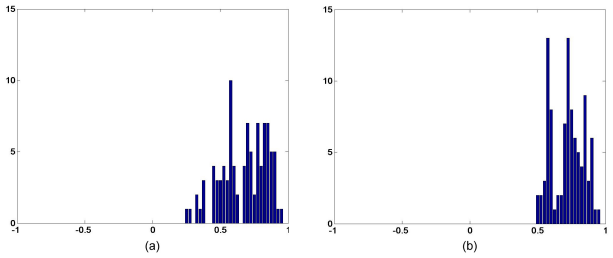

Fig. 6. Histograms of det(J) for elements of the prostate mesh (a) before element quality optimization and (b) after element quality optimization

are varied in an optimization procedure that maximizes the element's det(J) value. The optimization algorithm applied is a Nelder-Mead simplex search [26].

Because the mesh is constructed with medial object (u, v, t, τ) coordinates, but node positions do not actually have four degrees of freedom, coordinate transforms are applied in the optimization process. For nodes in the interior of a figure the parameters optimized are (A, B, C) coordinates, whose derivation from (u, v, t, τ) coordinates is explained in the appendix. (A, B, C) coordinates are better for the optimization purpose than (x, y, z) world coordinates because they are closely based on the medial object coordinates and the mapping between (u, v, t, τ) and (A, B, C) is easily invertible, unlike the mapping between (u, v, t, τ) and (x, y, z). For nodes on the surface of a figure the parameters optimized are (a, b). The derivation of the (a, b) to (u, v, t, τ) coordinate mapping is also given in the appendix. Optimization in this two-dimensional parameter space implicitly constrains surface nodes to remain on the surface. The benefit of using these coordinate transformations in the optimization process is that the number of coordinate variables needed to specify node positions is reduced, thereby making the optimization process more robust and efficient.

This optimization process successfully produced a hexahedral prostate mesh for which det(J) > 0.5 for all elements. This mesh is shown in Fig. 7, and histograms of element quality before and after optimization are in Fig. 6.

D. Meshing Space External to M-reps

In a multi-object deformation problem the space between modeled objects needs to be meshed, and in a single object situation it is often useful to mesh space outside the modeled object so that a deformation can be applied to the surrounding space. The m-rep meshing algorithm does not address the problem of meshing non-modeled areas. Instead, a layer of pyramids is built on top of the hexahedral elements generated by the m-rep meshing algorithm so as to cause all the resulting exposed faces to be triangles. Then tetrahedra are used to fill the remainder of the volume of interest. The construction of the tetrahedral mesh is performed using the tetrahedral meshing capability found in CUBIT, a meshing program from Sandia National Laboratories. CUBIT takes the exposed surface triangles as input and provides a tetrahedral meshing as output. The pyramid and tetrahedral elements that fill the space external to the models are shown in Figs. 7 and 7e.

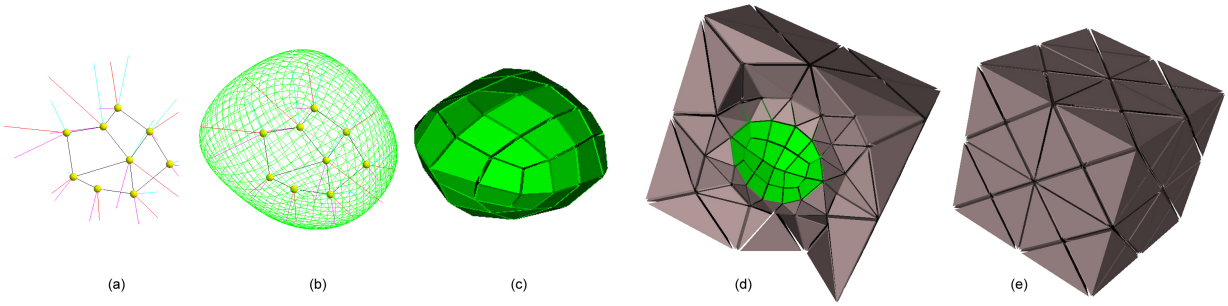

Fig. 7. (a) M-rep model of a prostate (b) Prostate m-rep with implied surface (c) Base level prostate mesh (d) Sliced view of the meshed volume of interest (e) Exterior view of the meshed volume of interest

III. Boundary Conditions

A. Initial Approximation

In order to compute a deformation with finite element analysis, boundary conditions must be specified for some of the nodes either in terms of forces applied to the nodes or node displacements.

With an image registration problem, neither forces nor point displacements are available directly from the images. What is visible in the images is shifting and/or change in the shape of the object boundary. M-reps provide a way to derive an initial approximation to point displacements from observed boundary changes in an image.

In the prostate case, the m-rep model that was fitted to the original image and used to guide mesh construction is transferred onto the image of the deformed prostate and automatically fit to it. The original and deformed m-rep models have the same topology, and their object based coordinates span exactly the same parameter space. This means that the m-rep's object based coordinate system defines a one to one geometry based correspondence between points in the original and deformed prostate, as illustrated in Fig. 3. For each surface node with medial coordinates (u_i, v_i, t_i, τ_i) the approximate displacement vector d_i is defined in the following way.

$$\begin{aligned} \left[\, x_i \;\; y_i \;\; z_i \,\right] &= MedialToWorld(model, u_i, v_i, t_i, \tau_i) \\ \left[\, x_i' \;\; y_i' \;\; z_i' \,\right] &= MedialToWorld(model', u_i, v_i, t_i, \tau_i) \\ d_i &= \left[\, x_i' \;\; y_i' \;\; z_i' \,\right] - \left[\, x_i \;\; y_i \;\; z_i \,\right] \end{aligned} \tag{4}$$

The nodes on the exterior surface of the whole meshed volume are assumed to be fixed, so their displacements are set to 0. These exterior surface nodes are the ones lying on the outermost faces of the tetrahedra seen in Fig. 7e.

Using this set of boundary conditions will result in a deformed object that evidences the shape change observed in the image and captured by the m-rep. However, this geometry based approximation of the boundary conditions is not the only set of boundary conditions that accomplishes the desired shape change. In order to improve the accuracy of the computed deformation the boundary conditions applied to the surface of the modeled object(s) are optimized so that the energy of the deformation is minimized, as described in section III.B.

B. Boundary Condition Optimization

We assume that given multiple sets of boundary conditions that result in the observed boundary shape change, the most likely set is associated with the deformation that requires the least amount of energy.

The boundary conditions are applied only to nodes lying on an object surface, so the optimization is most efficiently performed using the nodes' (a, b) surface coordinates that are explained in the appendix. For the i^{th} surface node, (a_i, b_i) references a point on the surface of the original $model$ and (a_i', b_i') denotes a point on the surface of the deformed $model'$. The displacement d_i is defined as follows:

$$\begin{aligned} \left[\, x_i \;\; y_i \;\; z_i \,\right] &= SurfaceToWorld(model, a_i, b_i) \\ \left[\, x_i' \;\; y_i' \;\; z_i' \,\right] &= SurfaceToWorld(model', a_i', b_i') \\ d_i &= \left[\, x_i' \;\; y_i' \;\; z_i' \,\right] - \left[\, x_i \;\; y_i \;\; z_i \,\right] \end{aligned} \tag{5}$$

The $SurfaceToWorld$ transform involves mapping the (a, b) coordinates to medial (u, v, t, τ) coordinates using the relations detailed in the appendix, and then applying the $MedialToWorld$ transform to the (u, v, t, τ) coordinates.

Initially (a_i', b_i') = (a_i, b_i). In the optimization process the (a_i', b_i') coordinates are adjusted by a Nelder-Mead simplex search optimization algorithm [26] so that the energy of the resultant deformation is minimized. The variation of the a' and b' coordinates is illustrated in Fig. 8.

The energy of a linear elastic deformation, also known as the strain energy, is defined as follows [27] [28]:

$$PE = \frac{1}{2}\int_V \sigma \cdot \varepsilon \; \mathrm{d}V \quad \text{where} \quad \begin{array}{ll} \sigma & \text{is the stress} \\ \varepsilon & \text{is the strain} \end{array} \tag{6}$$

For the prostate phantom registration problem, the boundary condition optimization resulted in a 20% reduction in the energy of the deformation and an average change of 1.2 mm in the optimized boundary displacement vectors that were applied to nodes on the prostate surface. Registration error estimates for both optimized and unoptimized boundary conditions are provided in section V Table I. Interestingly, the boundary condition optimization had a negligible impact on the accuracy of the deformation for points in the interior of the prostate. A possible explanation for the boundary condition optimization not resulting in improvement in the accuracy of the prostate deformation is that the m-rep prediction algorithm

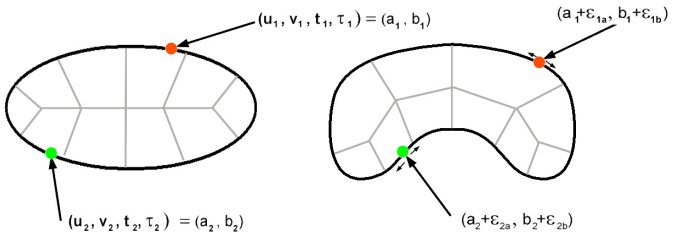

Fig. 8. In the boundary condition optimization process, (u, v, t, τ) coordinates are converted to the more compact (a, b) surface coordinates. Corresponding points are then allowed to slide along the object surface, as shown on the right, to minimize the energy of a deformation.

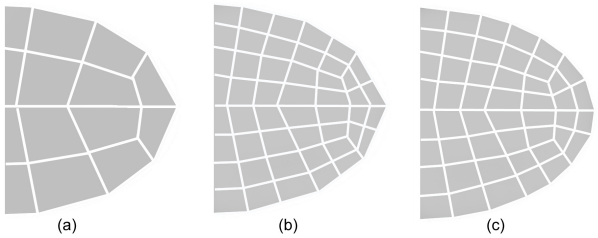

Fig. 9. (a) Coarse mesh. (b) Subdivision of coarse mesh using Euclidean coordinate midpoint computations. (c) Subdivision of coarse mesh using medial coordinate midpoint computations. The subdivision in (c) is a smoother approximation of the object's boundary than the subdivision in (b).

may provide a sufficiently accurate boundary condition estimate for deformations that involve little or no torsion or other complicated warp. Further testing of the boundary prediction algorithm with a variety of objects and deformations will be useful in determining the limits of the algorithm's reliability.

IV. Solution Algorithm

A. Solution on the Initial Mesh

To compute the deformation of a three dimensional object, a $3N \times 3N$ finite element system of linear equation must be solved, where N is the number of nodes in the object's mesh. An initial approximation to the solution can be derived from the m-rep model correspondences in the same way that the initial approximation to the boundary conditions was derived. For each node n_i in the mesh, an initial approximation to the node's displacement vector d_i is defined by equation 3. A preconditioned conjugate gradient solver is used to iteratively improve the initial approximate solution.

B. Mesh Subdivision

If accuracy greater than that provided by the initial coarse mesh is desired, the initial mesh can be subdivided. The result is a mesh with smaller elements that provides a finer representation of the solution.

The hexahedral elements that represent the m-rep modeled objects have nodes with both world space (x, y, z) coordinates and medial (u, v, t, τ) coordinates. By subdividing these elements using their medial node coordinates, an improved, smoother approximation to the object geometry is achieved with the subdivided mesh. Straightforward subdivision with world space coordinates would provide better resolution for representing the solution but would have the same error in its geometric representation. The medial coordinate based subdivision process allows for increased precision in both the geometry and the solution. The advantage of increased geometric precision is a reduction in deformation error in the vicinity of the boundary. Subdivision using world space coordinates is compared to subdivision using medial object coordinates in Fig. 9.

The result of applying medial coordinate based subdivision to a prostate mesh is shown in Fig. 10. The size of a mesh grows quickly with subdivision, as shown by the node and element counts reported for each mesh level in Fig. 11. For

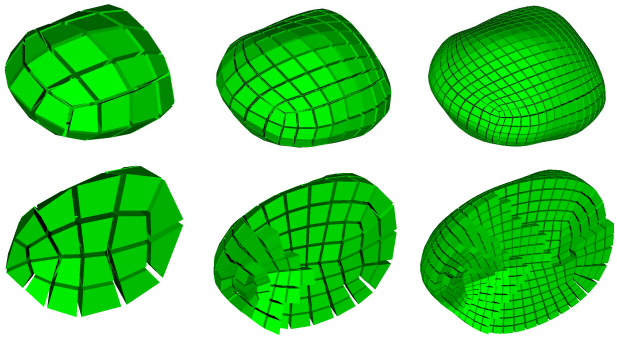

Fig. 10. Top row: Surface of a prostate mesh at subdivision levels 1 - 3 Bottom row: Sliced view of a prostate mesh at subdivision levels 1 - 3

prostate meshes, the element shape quality remained high after two subdivision steps. However, if an m-rep model had areas of very high surface curvature, element shape quality could be degraded through subdivision using medial object coordinates. In this case mesh quality optimization as described in section II.C could be applied to subdivided mesh levels. In practice this has not been necessary for the prostate application.

C. Solution on a Subdivided Mesh

The system of equations that results from a subdivided mesh is much larger than the original system of equations. The increase in the node count at each subdivision level can be seen in Fig. 11. The new larger system of equations can be efficiently solved by taking a multiscale approach and using sparse matrix data structures.

The approach taken here is to solve the finite element system of equations on the initial mesh using the procedure outlined in section IV-A and then interpolate that solution to the subdivided mesh and solve again using a conjugate gradient solver. The number of iterations required to converge to a solution is reduced due to the good initial approximation provided by the solution on the coarser mesh. The subdivision - interpolation - solution process may be repeated as many times as desired to get an increasingly fine representation of the geometry and solution. In practice two or three mesh levels have provided sufficient accuracy for the prostate deformation problem. Fig. 11 shows the number of conjugate gradient iterations required for solution convergence at three subdivision levels and shows that the computational savings gained by starting with the m-rep predicted solution increases with the subdivision level.

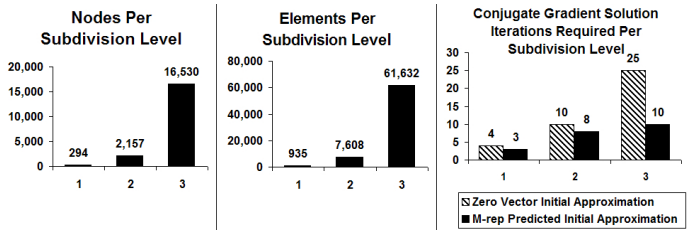

Fig. 11. The number of nodes, elements, and solution iterations for prostate mesh subdivision levels 1 - 3. The rightmost graph compares the solution iteration counts required using a zero displacement initial solution approximation compared to the iteration counts required using m-rep predicted displacements as the solution approximation.

V. Registration Experiment

Because the clarity and resolution of CT images are superior to MRSI and ultrasound images, the initial validation study was performed using CT prostate images. CT images were acquired at Memorial Sloan-Kettering Cancer Center of a male pelvis phantom with an inflated and deflated MRSI probe in the phantom rectum. The phantom prostate was implanted with seeds, so the accuracy of the computed deformation can be examined by comparing the computed seed displacements with the observed seed displacements. For this experiment, the single object prostate m-rep model was used and the area around the prostate was represented as a homogeneous region.

The linear elastic model has two elastic constants that describe a material's deformable characteristics: E, Young's modulus, and ν, Poisson's ratio. In this experiment, the effect of forces applied to the prostate was captured by displacement type boundary conditions. Since no force type boundary conditions were specified, the deformation did not depend on Young's modulus [22]. The prostate was assigned $\nu = .495$, indicating near incompressibility. The meshed area exterior to the prostate was assigned $\nu = 0.3$.

A view through the center of the deformed base level prostate mesh is shown in Fig. 12. In Fig. 14 the computed deformation is applied to a slice of the phantom's CT.

The locations of 75 seeds implanted in the phantom prostate were identified manually in both the uninflated and inflated CT images with 0.7 mm within slice resolution and 3 mm slice thickness. The average amount of seed movement due to the inflation of the MRSI imaging probe was 9.4 mm. Seeds lying next to the rectum experienced moved more than seeds further from the rectum; the 25 seeds closest to the rectum moved an average of 11.6 mm. The accuracy of the manual seed labelling was limited by the image resolution.

The computed deformation was applied to seed locations in the uninflated image to predict seed locations in the inflated image. The predicted seed locations were then compared to observed seed locations in the inflated image. The results of this comparison are given in Table I and Fig. 13. Fig. 15 contains histograms of the x, y, and z components of the error estimates. Registrations computed using the second and third level prostate meshes met the goal of 2 mm registration error.

The component of registration error in the lower resolution z direction is significantly larger than the x and y error components. This is due to seed segmentation error that contributed to the registration error estimate. It was not possible to separate the error due to segmentation from the error due to inaccuracies in the deformation.

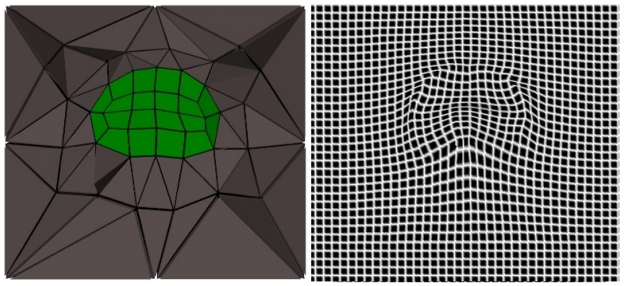

Fig. 12. Left: A slice through the meshed prostate volume after the deformation has been computed. The mesh shown has not been subdivided. Right: The computed deformation applied to a regular grid.

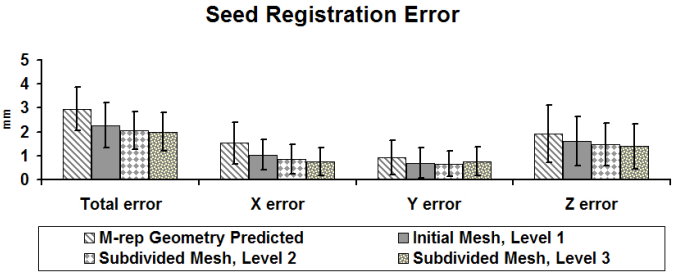

Fig. 13. Average seed registration error is graphed for the group of 75 implanted seeds in the prostate phantom. For the directional components of the error, horizontal bars indicate the CT voxel size in that direction. The "m-rep predicted" category shows how well the m-rep geometry based correspondences registered the seeds without the use of finite element modeling.

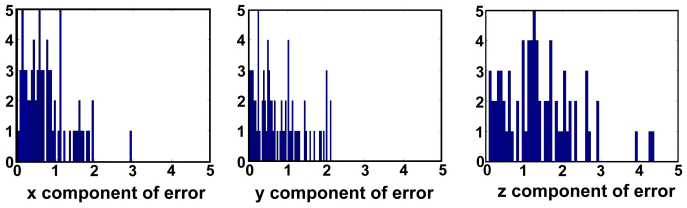

Fig. 15. Histograms of the separated x, y, and z components of the error estimates for predicted seed locations in the Uninflated → Inflated mapping are shown. The horizontal axis is millimeters of registration error.

The tissue nearest the rectum deforms the most due to intra-rectal probe inflation. Larger deformations are more nonlinear, so the actual deformation deviates most strongly from the predictions of a linear elastic model in the area of largest deformation. This is evidenced by the graph in Fig. 16 that compares the registration accuracy of the entire group of seeds to the registration accuracy of the seeds nearest the rectum.

Since the finite element code used for this experiment was implemented in Matlab, execution times could be improved with a compiled and optimized implementation of the algorithms presented. With the current implementation, a deformation of prostate mesh level 1 or 2 could be computed on a desktop workstation in several minutes. A solution on mesh level 3 required about 12 hours. Given the large difference in computation time and the small difference in accuracy between the second and third level meshes, the second level mesh is the best choice for prostate registration.

TABLE I

THE ERROR ESTIMATES LISTED ARE FOR THE UNINFLATED PROBE → INFLATED PROBE PROSTATE IMAGE MAPPING AND ARE BASED ON THE DIFFERENCE BETWEEN (A) THE OBSERVED SEED LOCATIONS IN THE INFLATED IMAGE AND (B)THE PREDICTED SEED LOCATIONS THAT RESULT FROM APPLYING THE COMPUTED DEFORMATION TO THE SEED LOCATIONS IN THE UNINFLATED IMAGE. ERRORS ARE IN MILLIMETERS AND REPRESENT AVERAGES OVER ALL 75 SEEDS. x AND y COMPONENTS LIE IN A .07MM RESOLUTION IMAGE PLANE. THE z COMPONENT LIES ACROSS IMAGE PLANES WITH A 3MM SPACING.

	Mesh Level	total error	total std. dev.	x error	x std. dev.	y error	y std. dev.	z error	z std. dev.
unoptimized	1	2.273	0.934	1.043	0.642	0.696	0.641	1.608	1.036
boundary	2	2.044	0.790	0.857	0.617	0.666	0.534	1.474	0.893
conditions	3	1.999	0.808	0.763	0.580	0.764	0.599	1.392	0.930
optimized	1	2.705	0.869	1.308	0.785	1.026	0.776	1.730	1.057
boundary	2	2.054	0.799	0.852	0.605	0.679	0.547	1.485	0.900
conditions	3	2.000	0.807	0.766	0.580	0.761	0.598	1.393	0.928

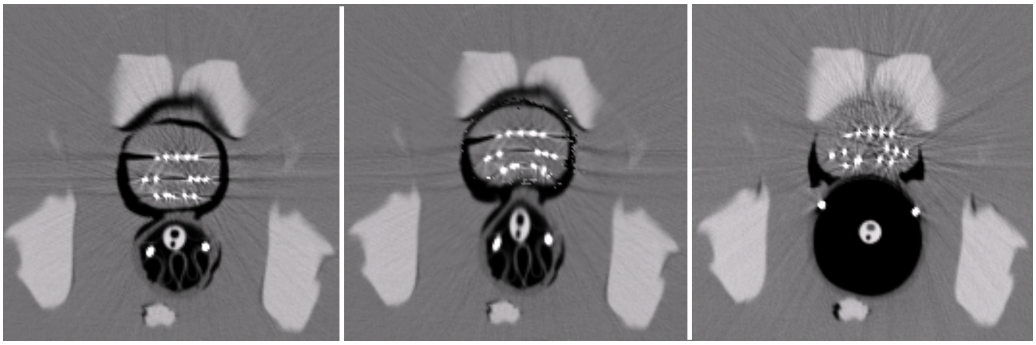

Fig. 14. Left: CT Slice of the phantom prostate with uninflated probe; Center: Same slice as left, after computed deformation has been applied; Right: CT slice of the phantom prostate with inflated probe. The goal was to register the prostate volume, not the bones, rectum, or surrounding tissue. Therefore only the prostate was explicitly modeled and the area outside the prostate was represented as a homogeneous region. No attempt was made to minimize the discrepancies in the registration outside the prostate.

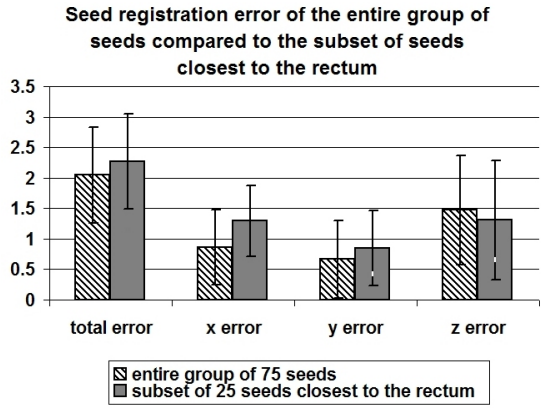

Fig. 16. Total average registration error for the entire group of seeds is less than for the subset of seeds nearest the rectum. Also in the x and y directions, for which the seed segmentations are most reliable, the seeds nearest the rectum have higher registration error.

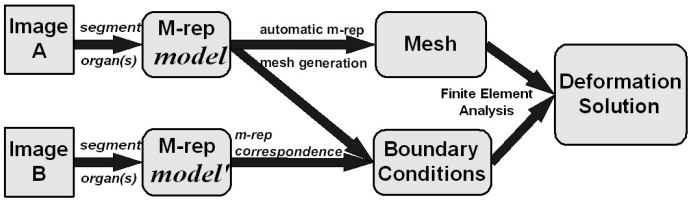

Fig. 17. These steps result in a deformation field that can be applied to Image A to register it with Image B.

VI. CONCLUSIONS AND FUTURE WORK

In summary, the steps of an automated, finite element based image registration algorithm have been described. M-rep shape models have been employed to link together the tasks of image segmentation, mesh construction, and boundary condition specification. Fig. 17 illustrates the flow of the registration algorithm.

The initial validation experiments have been conducted with prostate phantom CT images. This has enabled careful analysis of registration accuracy because the phantom provided a highly controlled environment and the CT images had higher resolution and clarity than typical MRSI and ultrasound clinical images. However, application of this methodology to clinical images is an important next step.

Clinical validation is complicated because it involves using a non-rigid image registration to guide brachytherapy seed placement. The errors in seed placement will depend both on registration errors and on needle insertion and guidance errors. Therefore a goal will be to show that seed placements observed in a post-operative image more closely match the pre-operative plan when the non-rigid image registration is applied intra-operatively to the treatment planning image.

For large deformations of the prostate, a hyperelastic or viscoelastic mechanical model may provide better registration results. A related research effort is aimed at modeling the way soft tissue deforms during needle insertion. Combining a

needle insertion model with non-rigid image registration may provide a highly precise method for designing and delivering brachytherapy treatment.

Future plans include the development of a local subdivision method that would allow a mesh to be refined in areas where the solution or geometry require higher resolution. This approach would be more computationally efficient than the global subdivision method currently in use.

Planned experiments also include the use of a five object male pelvis model that includes the rectum, bladder, and pubic bone objects in addition to the prostate. The use of a multi-object model would allow not only the prostate but also the surrounding structures to be accurately registered.

APPENDIX I
MEDIAL OBJECT COORDINATE TRANSFORMS

An m-rep figure is an inherently three-dimensional object, and its surface is inherently two-dimensional. However, medial object coordinates use four (u, v, t, τ) parameters. For efficiency, coordinate transforms are defined to map (u, v, t, τ) coordinates into the three-dimensional (A, B, C) parameter space and to map figure surface coordinates into the two-dimensional (a, b) parameter space.

An m-rep figure can be divided into five regions: a center region and four rim regions, labelled R_A, R_B, R_C, R_D and R_E in Fig. 18 (a). In any one of the regions only three of the four medial coordinates are needed to uniquely identify a point. For the entire center region, R_E, all points can be referenced by $(u, v, 1, \tau)$; t does not need to vary. In each rim region, either u or v maintains a constant value. Therefore, the (u, v, t, τ) parameter space can be viewed as five three-dimensional parameter spaces rather than as one four-dimensional space. The (A, B, C) parameter space simply maps these five three-dimensional segments into one continuous three-dimensional space. For the center region, the mapping is direct.

$$A = u \qquad B = v \qquad C = \tau \tag{7}$$

For the rim regions, a more complicated mapping is necessary because the t and τ medial object coordinates for the rims are essentially polar coordinates, while the (A, B, C) coordinates form an object based Cartesian type coordinate system. (See Fig. 18 (c) and (d)) The (A, B, C) coordinates for each rim span a wedge shaped region, as shown in Fig. 18 (b). The equations of the $(u, v, t, \tau) \rightarrow (A, B, C)$ mapping for each rim region are as follows.

$$\begin{aligned}
\alpha &= \frac{1}{\tan\left(\frac{t\pi}{2}\right) + 1} \\
R_A: \; A &= v\,(1 - |\tau|\alpha) + (1 - v)(-|\tau|\alpha)\left(\frac{u_{max} + 1}{u_{max} - 1}\right) \\
B &= v \\
R_B: \; A &= u \\
B &= (u_{max} + 1 - u)\,(v_{max} + |\tau|\alpha) \\
&\quad + (u - u_{max})(v_{max} - 1 + |\tau|\alpha)\left(\frac{v_{max} + 1}{v_{max} - 1}\right) \\
R_C: \; A &= (v_{max} + 1 - v)\,(u_{max} + |\tau|\alpha) \\
&\quad + (v - v_{max})(u_{max} - 1 + |\tau|\alpha)\left(\frac{u_{max} + 1}{u_{max} - 1}\right) \\
B &= v \\
R_D: \; A &= u \\
B &= u\,(1 - |\tau|\alpha) + (1 - u)(-|\tau|\alpha)\left(\frac{v_{max} + 1}{v_{max} - 1}\right) \\
R_A,\; R_B,\; R_C, R_D: & \\
C &= \tau\,(1 - \alpha)
\end{aligned}$$

(a, b) medial object surface coordinates are defined using the (A, B, C) coordinates described above. The (a, b) parameter space is basically the surface of the (A, B, C) parameter space unfolded along the $(u_{max} + 1)$ edge.

$$\begin{aligned}
a &= \begin{cases} A & \text{if } C \geq 0 \\ 2\,(u_{max} + 1) - A & \text{if } C < 0 \end{cases} \\
b &= B
\end{aligned}$$

ACKNOWLEDGMENT

We thank Gregg Tracton for assistance with image processing and Gilad Cohen for the prostate phantom design.

REFERENCES

[1] A. Bharatha, M. Hirose, N. Hata, S. Warfield, M. Ferrant, K. Zou, E. Suarez-Santana, J. Ruiz-Alzola, A. D'Amico, R. Cormack, R. Kikinis, F. Jolesz, and C. Tempany, "Evaluation of three-dimensional finite element-based deformable registration of pre-and intraoperative prostate imaging," *Medical Physics*, vol. 28, pp. 2551–2560, Dec 2001.

[2] A. Mohamed, C. Davatzikos, and R. Taylor, "A combined statistical and biomechanical model for estimation of intra-operative prostate deformation," *Proceedings, Medical Image Computing and Computer-Assisted Intervention (MICCAI), Part II*, pp. 452–460, 2002.

[3] M. Ferrant, A. Nabavi, B. Macq, F. A. Jolesz, R. Kikinis, and S. K. Warfield, "Registration of 3-D MR images of the brain using a finite element biomechanical model," *IEEE Transactions on Medical Imaging*, vol. 20, no. 12, pp. 1384–1397, 2001.

[4] S. K. Kyriacou, C. Davatzikos, S. J. Zinreich, and R. N. Bryan, "Nonlinear elastic registration of brain images with tumor pathology using a biomechanical model," *IEEE Transactions on Medical Imaging*, vol. 18, no. 7, pp. 580–592, 1999.

[5] A. Hagemann, K. Rohr, H. S. Stiehl, U. Spetzger, and J. M. Gilsbach, "Biomechanical modeling of the human head for physically based, nonrigid image registration," *IEEE Transactions on Medical Imaging*, vol. 18, no. 10, pp. 875–884, October 1999.

[6] M. H. Xu and W. L. Nowinski, "Talairach-Tournoux brain atlas registration using a metalforming principle-based finite element method," *Medical Image Analysis*, vol. 5, pp. 271–279, 2001.

[7] F. Azar, D. N. Metaxas, and M. D. Schnall, "A deformable finite element model of the breast for predicting mechanical deformations under external perturbations," *Journal of Academic Radiology*, vol. 8, pp. 965–975, October 2001.

[8] A. Samani, J. Bishop, M. J. Yaffe, and D. B. Plewes, "Biomechanical 3-D finite element modeling of the human breast using mri data," *IEEE Transactions on Medical Imaging*, vol. 20, no. 4, pp. 271–279, April 2001.

[9] M. Chabanas and Y. Payan, "A 3D finite element model of the face for simulation in plastic and maxillo-facial surgery," *Proceedings, Third International Conference on Medical Image Computing and Computer-Assisted Intervention (MICCAI)*, pp. 1068–1075, 2000.

[10] S. Cotin, H. Delingette, and N. Ayache, "Real-time elastic deformations of soft tissues for surgery simulation," *IEEE Transactions On Visualization and Computer Graphics*, vol. 5, no. 1, pp. 62–73, Jan-Mar 1999.

[11] R. J. Lapeer and R. W. Prager, "Finite element model of a fetal skull subjected to labour forces," *Proceedings, Second International Conference on Medical Image Computing and Computer-Assisted Intervention (MICCAI)*, pp. 1143–1155, 1999.

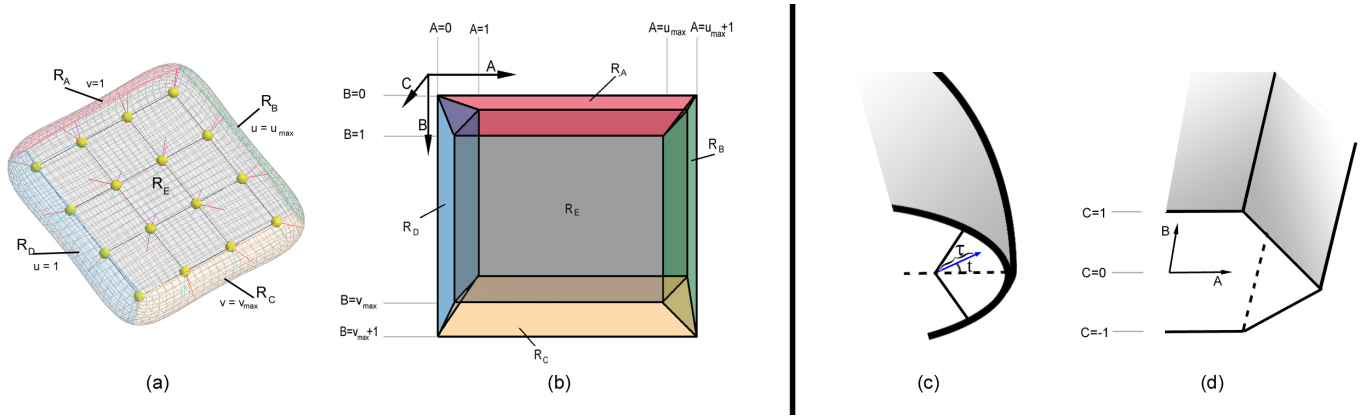

Fig. 18. (a) Five regions of an m-rep figure (b) Diagram of the (A, B, C) parameter space with the five m-rep regions labelled (c) & (d) A sliced view of one of the rim regions, with the polar type medial object coordinates shown on the left and the corresponding (A, B, C) parameter space on the right.

[12] V. Narayana, P. L. Roberson, R. J. Winfield, and P. W. McLaughlin, "Impact of ultrasound and computed tomography prostate volume registration on evaluation of permanent prostate implants," *International Journal of Radiation Oncology Biology Physics*, vol. 39, no. 2, pp. 341–346, 1997.

[13] M. V. Herk, A. Bruce, A. P. G. Kroes, T. Shouman, A. Touw, and J. V. Lebesque, "Quantification of organ motion during conformal radiotherapy of the prostate by three dimensional imgae registration," *International Journal of Radiation Oncology Biology Physics*, vol. 33, no. 5, pp. 1311–1320, 1995.

[14] B. W. Fei, C. Kemper, and D. L. Wilson, "A comparative study of warping and rigid body registration for the prostate and pelvic MR volumes," *Computerized Medical Imaging and Graphics*, vol. 27, no. 4, pp. 267–281, 2003.

[15] M. Hirose, A. Bharatha, N. Hatga, K. H. Zou, S. K. Warfield, R. A. Cormack, A. D'Amico, R. Kikinis, F. A. Jolesz, and C. M. Tempany, "Quantitative MR imaging assessment of prostate gland deformation before and during MR imaging-guided brachytherapy," *Academic Radiology*, vol. 9, no. 8, pp. 906–912, August 2002.

[16] H. Blum and R. Nagel, "Shape description using weighted symmetric axis features," *Pattern Recognition*, vol. 10, pp. 167–180, 1978.

[17] S. M. Pizer, J. Z. Chen, P. T. Fletcher, Y. Fridman, D. S. Fritsch, A. G. Gash, J. M. Glotzer, M. R. Jiroutek, S. Joshi, C. Lu, K. E. Muller, A. Thall, G. Tracton, P. Yushkevich, and E. L. Chaney, "Deformable m-reps for 3D medical image segmentation," *International Journal of Computer Vision*, vol. 55, no. 2/3, pp. 85–106, 2003.

[18] S. E. Benzley, E. Perry, K. Merkley, B. Clark, and G. Sjaardama, "A comparison of all hexagonal and all tetrahedral finite element meshes for elastic and elasto-plastic analysis," *Proceedings, 4th International Meshing Roundtable*, pp. 179–191, October 1995.

[19] B. Couteau, Y. Payan, and S. Lavallee, "The mesh-matching algorithm: an automatic 3D mesh generator for finite element structures," *Journal of Biomechanics*, vol. 33, pp. 1005–1009, 2000.

[20] R. Schneiders, "Quadrilateral and hexahedral element meshes," in *Handbook of Grid Generation*, J. F. Thompson, B. K. Soni, and N. P. Weatherill, Eds. Florida: CRC Press, 1998.

[21] J. Crouch, S. Pizer, E. Chaney, and M. Zaider, "Medially based meshing with finite element analysis of prostate deformation," *Medical Image Computing and Computer Assisted Intervention*, 2003.

[22] J. Crouch, *Medial Techniques for Automating Finite Element Analysis*. dissertation, UNC-Chapel Hill department of computer science, 2003. [Online]. Available: http://midag.cs.unc.edu/pubs/phd-thesis/JCrouch03.pdf

[23] Department of Mechanics and Materials, Lund University, *CALFEM, a finite element toolbox to MATLAB*, Lund, Sweden, 1999. [Online]. Available: http://www.byggmek.lth.se/Calfem/Calman/pdfcalfem.pdf

[24] K. Bathe, *Finite Element Procedures*. New Jersey: Prentice-Hall, 1996.

[25] P. Knupp, "Hexahedral mesh untangling and algebraic mesh quality metrics," *Proceedings, 9th International Meshing Roundtable*, pp. 173–183, October 2000.

[26] J. Lagarias, J. Reeds, M. Wright, and P. Wright, "Convergence properties of the Nelder-Mead simplex method in low dimensions," *SIAM Journal of Optimization*, vol. 9, no. 1, pp. 112–147, 1998.

[27] Y. Fung and P. Tong, *Classical and Computational Solid Mechanics*. World Scientific Publishing Company, 2001.

[28] P. G. Ciarlet, *Mathematical Elasticity Volume 1: Three-dimensional elasticity*. Amsterdam: Elsevier Science Pubishers, 1988.

Jessica Crouch received a Ph.D. in computer science in 2003 and master's degree in computer science in 1999, both from from the University of North Carolina at Chapel Hill. Her Bachelor's degree, also in computer science, is from the University of Richmond. She is currently a Postdoctoral Fellow in the Engineering Research Center at The Johns Hopkins University in Baltimore, Maryland, and is involved in collaborative research with Memorial Sloan-Kettering Cancer Center.

Stephen M. Pizer is Kenan Professor of Computer Science, Radiology, Radiation Oncology and Biomedical Engineering at the University of North Carolina, Chapel Hill. His Bachelor degrees are from Brown University, in Applied Mathematics, and his Ph.D. is from Harvard University in 1967, in Computer Science. Dr. Pizer heads UNCs multi-departmental Medical Image Display and Analysis Group, a collaborative research group of over 100 professionals. His recent research focus has been on medial models of the geometry of objects and multi-object complexes and the use of these models in 3D image segmentation and statistical characterization of object geometry.

Edward L. Chaney is the head of the Physics and Computing Division of the Department of Radiation Oncology at the University of North Carolina at Chapel Hill. He received his PhD in physics from the University of Tennessee in 1969 and his Bachelor's in physics from Milsaps College in 1965. His research interests include the development of new techniques for image guided radiotherapy treatment planning and verification as well as translational research involving migration of imaging research into clinical systems. Current research is focused on deformable medial models for image segmentation to define normal anatomical structures; registration of volumetric images for tumor localization; and analysis of portal images to measure treatment field shape and to detect treatment setup errors.

Dr. Marco Zaider is the Head of Brachytherapy Physics at Memorial Sloan-Kettering Hospital and Professor of Physics (Radiology) at Cornell Medical School. His research interests include microdosimetry, interaction of ionizing radiation with biomolecules (DNA), algorithms for treatment plan optimization and biophysical modeling of radiation effects.